# Influence of Vacancies in Manganese Hexacyanoferrate Cathode for Organic Na-Ion Batteries: A Structural Perspective

Min Li,[a] Mattia Gaboardi,[b] Angelo Mullaliu,[c, d] Mariam Maisuradze,[a] Xilai Xue,[c, d] Giuliana Aquilanti,[b] Jasper Rikkert Plaisier,[b] Stefano Passerini,*[c, d, e] and Marco Giorgetti*[a]

Manganese hexacyanoferrates (MnHCF) are promising positive electrode materials for non-aqueous batteries, including Na-ion batteries, due to their large specific capacity ($> 130\ mAh\,g^{-1}$), high discharge potential and sustainability. Typically, the electrochemical reaction of MnHCF associates with phase and structural changes, due to the Jahn-Teller (JT) distortion of Mn sites upon the charge process. To understand the effect of the MnHCF structure on its electrochemical performance, two MnHCF materials with different vacancies content are investigated herein. The electrochemical results show that the sample with lower vacancy content (4%) exhibits relatively higher capacity retention of 99.1% and 92.6% at $2^{nd}$ and $10^{th}$ cycles, respectively, with respect to 97.4% and 79.3% in sample with higher vacancy content (11%). Ex-situ X-ray absorption spectroscopy (XAS) and ex situ X-ray diffraction (XRD) characterization results show that a weaker cooperative JT-distortion effect and relatively smaller crystal structure modification occurred for the material with lower vacancies, which explains the better electrochemical performance in cycled electrodes.

## Introduction

Metal hexacyanoferrates, also known as Prussian blue analogues (PBAs), are considered as promising positive electrode materials due to their large ionic channels and interstices in the lattice, abundant redox-active sites, and robust structural stability.[1–5] Among the various PBAs, manganese hexacyanoferrate ($A_xMn[Fe(CN)_6]_{1-y}\square_y\cdot H_2O$, where A: alkali metal ions, $0 \leq x \leq 2$; $\square$: $Fe(CN)_6$ vacancies, $y < 1$) has drawn a particular attention

[a]  M. Li, M. Maisuradze, Prof. Dr. M. Giorgetti
    Department of Industrial Chemistry
    University of Bologna
    Viale Risorgimento 4, 40136 Bologna (Italy)
    E-mail: marco.giorgetti@unibo.it
[b]  Dr. M. Gaboardi, Dr. G. Aquilanti, Dr. J. Rikkert Plaisier
    Elettra - Sincrotrone Trieste
    s.s. 14, km 163.5, Basovizza 34149, Trieste (Italy)
[c]  Dr. A. Mullaliu, X. Xue, Prof. Dr. S. Passerini
    Helmholtz Institute Ulm (HIU)
    Helmholtzstrasse 11, 89081, Ulm (Germany)
[d]  Dr. A. Mullaliu, X. Xue, Prof. Dr. S. Passerini
    Karlsruhe Institute of Technology (KIT)
    P.O. Box 3640, 76021 Karlsruhe (Germany)
    E-mail: stefano.passerini@kit.edu
[e]  Prof. Dr. S. Passerini
    Department of Chemistry
    Sapienza University of Rome
    Piazzale A. Moro 5, 00185 Rome (Italy)

and used as positive electrode (cathode) material for Li-ion,[1,6] Na-ion,[4,7] K-ion,[8,9] Mg-ion,[10,11] Zn-ion[12] and Al-ion[13] batteries, because it is composed of abundant and nontoxic elements and displays large reversible capacities ($> 120\ mAh\,g^{-1}$) due to the both active redox couples ($Fe^{3+}/Fe^{2+}$ and $Mn^{3+}/Mn^{2+}$) and high potentials ($> 3.4\ V$) in aprotic electrolytes.[14,15] However, manganese hexacyanoferrate (abbreviated as MnHCF in the following) suffers from poor cycling stability, i.e., capacity retention problems upon cycling, due to phase changes and the Jahn-Teller (JT) distortion[14–16] as most Mn-containing electrode materials, for example, $MnO_2$,[17,18] Li/NaMnO$_2$/ LiMn$_2$O$_4$/ Na$_4$Mn$_3$(PO$_4$)$_2$(P$_2$O$_7$).[19–22]

Stabilizing the crystal structure and mitigating the JT distortion during the charge/discharge process are crucial for applying Mn-containing electrode materials in practical devices. So far, different methods have been reported for MnHCF to enhance the battery performance, for example, partially replacing Mn with Jahn-Teller-inactive $Fe^{3+}$, $Co^{2+}$, or $Ni^{2+}$,[23–25] synthesizing core-shell structure manganese ferrocyanide (MnPB@NiPB),[26] and controlling the structure of MnHCF to obtain a high-performance cubic phase.[27] The local structure modifications occurring in the PBAs network upon Li/Na extraction has been reported by Giorgetti and coworkers,[15,28] showing as the cation removal from the MnHCF structure upon charge introduces an asymmetry in the Mn sites triggering $\approx 10\%$ Mn–N equatorial distance contraction, whereas the axial Mn–N distances remain roughly constant.[15] By considering the MnHCF Li-ion battery only,[28] X-ray diffraction (XRD) results show that the cell parameters $b$ and $c$ remain almost unchanged, but the cell parameter $a$ changes about 0.6% during the charge/discharge process. The lattice volume variation was about 2% upon the first electrochemical alkali-ion removal and insertion, which was apparently inconsistent with

the change of Mn–N distances (10%). This was explained with a non-cooperative Jahn-Teller effect, i.e., the JT-distortion of Mn sites mainly influences the localized orbital electronic states, but does not produce a macroscopic distortion in the long range. In this paper we intend to verify and extend this concept for the Na half-cell case by investigating the structure in cycled electrodes.

Generally, in the MnHCF structure, a vacancy portrays a missing $[Fe(CN)_6]^{4-}$ unit while the coordination of the unsaturated metal site is usually filled by a water molecule, which was thought to be detrimental to the battery stability performance. However, the presence of vacancies inside the structure might increase the ion conduction by generating additional diffusion pathways, especially for large inserted ions.[29,30] Goodenough and coworkers[16] reported the influence of the size, water content, and defectivity on the performance of KMnHCF as electrode material for Na-ion batteries. They showed that the optimized crystallinity and water (i.e., vacancies) content resulted in the highest specific capacity and the best cycle stability, even superior to those of the most crystalline and almost water-free material. Instead of $[Fe(CN)_6]^{4-}$ vacancies, Yang and coworkers[31] explored unconventional Mn vacancies ($V_{Mn}$) on the surface of Mn–Fe PBAs by utilizing a potent chelating agent. They found the $V_{Mn}$ in Mn–Fe PBAs can restrain the movement of Mn–N bonds and thereby mitigate the Jahn-Teller distortion of Mn–$N_6$ octahedra, leading to highly reversible phase transitions of Mn–Fe PBAs as well as outstanding long-term cycle stability and capacity retention.

In this work, the electrochemical performance in Na half-cells, and their crystalline phase and local atomic structure changes of two MnHCF samples with different $[Fe(CN)_6]^{4-}$ vacancies are comprehensively studied. The two MnHCF materials with the same phase (monoclinic), similar particle size, but different $[Fe(CN)_6]^{4-}$ vacancy content (4% and 11%) were synthesized and tested as cathode material in organic Na-ion battery. The results show that the sample with the lower vacancies content exhibits higher capacity retention (71.1% vs. 39.4%) after 100 cycles. Ex-situ X-ray absorption spectroscopy (XAS) and ex situ XRD results prove that both samples displayed a cooperative JT-distortion effect. Moreover, the sample with the lower vacancies content exhibits a more stable structural change and weaker JT-distortion effect on the Mn sites during the cycling.

## Experimental Section

### Synthesis of MnHCF

The synthesis of MnHCF is based on a simple and reproducible co-precipitation method, as reported in Ref. [27]. Briefly, Solution A [100 mL 0.1 M manganese sulfate monohydrate ($MnSO_4 \cdot H_2O$) solution] and Solution B [100 mL 0.1 M sodium ferrocyanide decahydrate {$Na_4Fe(CN)_6 \cdot 10H_2O$} solution] were simultaneously added dropwise to an aqueous solution of sodium sulfate ($Na_2SO_4$, 0.1 M 100 mL) by using a peristaltic pump at a rate of 4 mL min$^{-1}$. The reaction batch was kept under $N_2$ atmosphere at a constant temperature (40±2°C) by using a water bath. The obtained

solution was aged for five days, assuring complete decantation. Then, the precipitate was collected via centrifugation at 4000 rpm, washed three times with distilled water, and dried at 60°C for 48 h. This sample was labeled MnHCF-P (pristine). Another sample, labeled as MnHCF-A, was synthesized the same way as described above, with the addition of 0.1 M ascorbic acid (Powder, Sigma Aldrich) to Solution A. All chemicals from Sigma Aldrich were used as received without any further purification.

### Electrode preparation and electrochemical test

For electrode preparation, the cathode slurry was prepared by mixing 85 wt.% active material, 10 wt.% super C65 (IMERYS), and 5 wt.% PVDF (polyvinylidene difluoride; Solef 6020). PVDF was previously dissolved (10 wt.% solution) in N-methyl-2-pyrrolidone (NMP). The solid content of the slurry was 20 wt.%. The ball milling procedure consisted of two repetitions of 1 h each with a 10 min break between stages with a speed of the main disk of 400 r min$^{-1}$, and a relative speed planet of −800 r min$^{-1}$. The slurries were cast on the aluminum foil (thickness 20 μm, cleaned with ethanol before use and dried for two days at 80°C) using a blade coater (200 μm height of the wet slurry), and successively dried at 60°C for three days. Disk electrodes were cut using a Hohsen puncher with a diameter of 12 mm. The electrodes were pressed at 10 tons for 10 s and dried at 120°C under vacuum ($10^{-6}$ bar) for 24 h. Afterwards, all the electrodes were weighted in the dry room (dew point < −60°C). Before transfer to the Ar-filled glove box (MBRAUN MB 200B ECO), the electrodes were dried again at 120°C under the vacuum ($10^{-6}$ bar) for six hours. The areal loading of electrodes is around 2.10±0.11 mg cm$^{-2}$.

Electrochemical tests were conducted using three-electrode Swagelok-type cells including the MnHCF electrode as the working electrode while Na metal electrodes were used as the counter and reference electrodes. GF/D Whatman paper was used as a separator to avoid the direct electrical contact between the positive, negative, and reference electrodes. 1 M $NaPF_6$ in propylene carbonate (PC) was employed as the electrolyte. Galvanostatic cycling was performed using a Maccor battery tester 4000 within the 2.0–4.0 V (versus Na$^+$/Na) voltage range. The test always started from the open circuit potential with a positive polarization. The open circuit voltage (OCV) for both electrodes is around 3.0 V (vs. Na/Na$^+$). Cyclic voltammetry (CV) experiments were performed using a VMP multichannel potentiostat (Bio-logic) at a scan rate of 0.2 mV s$^{-1}$ between 2.0–4.0 V. All tests were performed in climatic chambers at 20±2°C.

### Characterization

Microwave plasma-atomic emission spectrometer (MP-AES) 4210 was used to detect the composition of the active material. During the test, three different wavelengths were chosen for each element.

Thermogravimetric analysis (TGA) was performed in an air atmosphere from room temperature to 500°C, with a heating rate of 5°C min$^{-1}$, and rapid cooling.

Infrared (IR) spectra were acquired with the Bruker Alpha FTIR spectrometer in ATR (attenuated total reflectance) mode in the spectral range of 4000–400 cm$^{-1}$.

XRD data were recorded by using a monochromatic X-ray beam at the MCX beamline at Elettra synchrotron, Trieste (Italy). The C1, D1, C2, D2 electrodes were tested under wavelength of 1.03318 Å, 12.0 keV, sealed with Kapton tape, while the new C2, C10 and D10 electrodes were tested under 0.6199 Å, 20.0 keV, sealed with Mylar. Powder data was collected in a capillary geometry, setting the

**ChemSusChem**

Research Article
doi.org/10.1002/cssc.202300201

**Chemistry
Europe**
European Chemical
Societies Publishing

spinner at 3000 rpm. Electrode samples were tested in the transition mode with a marCCD detector and scintillator detector. The XRD pattern was collected consecutively in the range of $5° < 2\theta < 50°$, with steps of $0.01°$ and an acquisition time of 1 s per step. The XRD data are presented in Q index, which is independent from the wavelength. The Q is calculated by $\frac{4\pi\sin\theta}{\lambda}$, where $\theta$ is the Bragg angle and $\lambda$ is the X-ray wavelength. The crystal structure was refined using GSAS-II software.[32]

XAS experiments were conducted at Elettra Synchrotron Trieste (Italy), at the XAFS beamline.[33] The storage ring was operated at 2.0 GeV in top-up mode with a typical current of 300 mA. Data were recorded at Fe and Mn K-edge in the transmission mode using ionization chambers filled with a mixture of Ar, $N_2$, and He to have 10%, 70%, and 95% absorption in the $I_0$, $I_1$, and $I_2$ chambers, respectively. Each scan used an internal reference of iron and manganese foil for the energy calibration. This allowed continuous monitoring of the energy during the consecutive scans. The white beam was monochromatized by using a fixed exit monochromator equipped with a pair of Si (111) crystals. Spectra were collected with a constant k-step of $0.3\ nm^{-1}$ with acquisition time 3 s per point from 6339 to 7100 eV, and from 6912 to 8087 eV around Mn and Fe K-edges, respectively. XAS primary data analysis was performed with the Athena program.[34]

## Results and Discussion

The chemical formulas of the prepared MnHCF powder materials were calculated based on MP-AES and TGA results, as shown in Figure 1a and Table 1. Compared with MnHCF-P, MnHCF-A, prepared using ascorbic acid, exhibits higher Na content, but lower vacancy content (4%) and water content. The $N_2$ atmosphere and ascorbic acid can effectively suppress the $Fe^{2+}/[Fe^{II}(CN)_6]^{4-}$ oxidation during the synthesis process. Meanwhile, the addition of ascorbic acid slows down the nucleation process resulting in a highly crystallized material.[35,36] The oxidation states of Mn and Fe were checked by X-ray photoelectron spectroscopy (XPS) (Figure S1). The peaks around 708.5 eV and 721.4 eV for Fe 2p and 641.8 eV and 653.9 eV for Mn 2P indicate the presence of $Fe^{2+}$ and $Mn^{2+}$, respectively.[12,37] The FTIR spectra show that the two samples share the same peaks (Figure 1b). The two small, but sharp peaks occurring at 3604 and $3532\ cm^{-1}$, as well as the intense one at $1620\ cm^{-1}$ are attributed to the —O—H stretching mode and the bending mode arising from the surface water and interstitial water. The most intense peak, appearing around $2065-2075\ cm^{-1}$, is the characteristic peak of the —C≡N group within the $Mn^{II}$—C≡N—$Fe^{II}$ chain.[29,30] The crystal structure characterization of the MnHCF materials was analyzed by synchrotron XRPD and the corresponding Rietveld refinement. MnHCF-P/A samples exhibit precisely the same peak patterns (Figure 1c), which are well-indexed into the monoclinic phase ($p2_1/n$) (Figure 1d and

Figure S2). The refined lattice parameters (a, b, c, and $\beta$) of MnHCF-P and MnHCF-A powder samples are quite close (Table 1), which indicates that even though they have different content of vacancies, the crystal structure in the long-range shows no apparent differences. The morphology of the two powder samples was checked by SEM, as shown in Figure S3. Both are composed of agglomerated small particles, some of which have a roughly cubic shape. The particle size measured from the cubic-shaped particles for MnHCF-P and MnHCF-A is approximately 1.0 μm and 1.5 μm, respectively.

XAS data of as-prepared MnHCF-P/A was recorded at Fe and Mn K-edge. The X-ray absorption near edge spectroscopy (XANES) and corresponding Fourier transform (FT) of $k^2$-weighted EXAFS (Extended x-ray absorption fine structure) signals are shown in Figure 1f–k. The XANES traces of MnHCF-P/A (Figure 1f, i) show overlapping spectra at both the Fe and Mn K-edges. When zooming in the pre-edge region, four pre-edge peaks for Fe and two pre-edge peaks for Mn are observed (Figure 1g, j), as previously reported.[15,38] The Fe K-edge spectra of MnHCF-P/A are totally overlapping. In addition, the Mn K-edge spectra of MnHCF-A are slightly shifted towards higher energies, around 0.1 eV (at normalized absorption of unity), which is not statistically significant, confirming their valence states should be in line with the surface ones from XPS data. The FT of Fe and Mn $k^2$-weighted EXAFS signals display three peaks related to the framework structure of MnHCF (the —Fe—C—N—Mn— chain, Figure 1h, k). Pair distances relative to the Fe—C—N—Mn structural network are summarized in Table S1.

The electrochemical performance of the MnHCF-P/A electrodes were examined in sodium metal cells, using 1 M $NaPF_6$ (PC) electrolyte within potential 2.0–4.0 V (vs. $Na^+/Na$). As shown in Figure 2a and b, the CV curves of the two MnHCF materials mainly exhibited one pair of redox peaks. The calculated potential difference between the anodic and cathodic peaks shows that MnHCF-A has a smaller potential difference ($\approx 0.15\ V$) than MnHCF-P ($> 0.30\ V$), supporting for a lower polarization of MnHCF-A during $Na^+$ insertion and extraction. The galvanostatic charge-discharge curves of the two materials are reported in Figure 2c and d. During the first cycle, the MnHCF-P and MnHCF-A electrodes exhibit one discharge plateau with discharge capacity of $144\ mAh\,g^{-1}$ and $146\ mAh\,g^{-1}$, respectively. During the second cycle, the capacity retention is 97.4% and 99.1% for MnHCF-P and MnHCF-A electrodes, respectively. After 10 cycles, the discharge plateau of MnHCF-P keeps almost the same potential (3.46 V), and the discharge capacity decreases to $110\ mAh\,g^{-1}$. For the MnHCF-A half-cell, the discharge potential plateau is seen at 3.45 V and the discharge capacity is $135\ mAh\,g^{-1}$. Although the two materials display very similar structural properties at beginning, clear differences are observed during the cycling, even after the

**Table 1.** Chemical composition and cell parameters (obtained from XRPD refinement results) of the MnHCF powder samples.

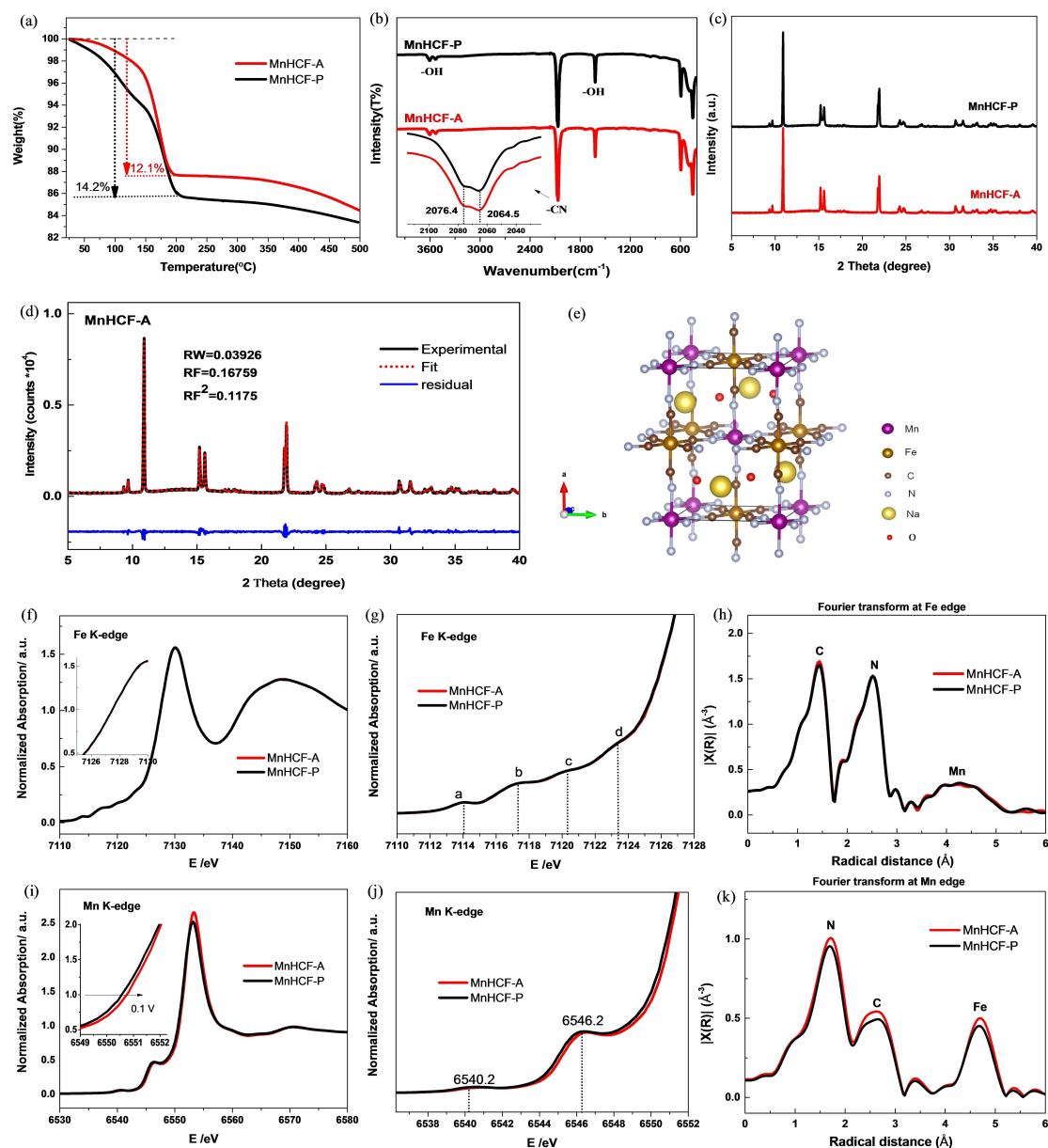| Powder | Chemical composition | a [Å] | b [Å] | c [Å] | β [°] |
|---|---|---|---|---|---|
| MnHCF-P | $Na_{1.41}Mn[Fe(CN)_6]_{0.89}\cdot 3.0\,H_2O$ | $10.547 \pm 0.010$ | $7.488 \pm 0.013$ | $7.370 \pm 0.012$ | $92.23 \pm 0.16$ |
| MnHCF-A | $Na_{1.65}Mn[Fe(CN)_6]_{0.96}\cdot 2.6\,H_2O$ | $10.584 \pm 0.014$ | $7.531 \pm 0.026$ | $7.339 \pm 0.025$ | $92.11 \pm 0.24$ |

**Figure 1.** (a) TGA curves of MnHCF-P/A; (b) IR spectra of MnHCF-P/A; (c) XRD patterns of MnHCF-P/A; (d) Rietveld refinement on MnHCF-A powder XRD data, as well as corresponding (e) crystal structure of MnHCF-A; XANES of MnHCF-P/A powders at Fe K-edge (f) and Mn K-edge (i); Magnification of the pre-edge feature of Fe K-edge (g) and Mn K-edge (j); (h, k) corresponding Fourier transform of Fe and Mn $k^2$-weighted EXAFS signal.

$1^{st}$ cycle. The capacity retention of MnHCF-A is 92.6% and 71.1% after 10 and 100 cycles, respectively. While for MnHCF-P only 79.3% and 39.4% of the initial capacity is left after 10 and 100 cycles, respectively (Figure 2e). There are several factors that can deteriorate the performance of hexacyanoferrates upon cycling. One of them is the water content, especially the interstitial water content. Even after extensive vacuum dehydration at 120°C, some $H_2O$ still remains inside the structure, which content is proportional to the vacancy content. The TGA analysis (Figure 1a) of initial powder sample shows that the content of interstitial water ($120°C < T < 200°C$) of MnHCF-P and MnHCF-A is 9.7% and 9.3%, respectively, which is not a significance difference. Another factor is the stability of crystal

structure of MnHCF-P and MnHCF-A, especially with the influence of JT distortion of the Mn sites during charge process, which is our focus here. Accordingly, to monitor any alteration concerning the crystal structure and the active metallic species, as well as the local atomic environment, specific techniques are required.

To monitor the local structural changes during the early stages of cycling, ex situ XAS spectra were collected at both Mn and Fe K-edge during the first two electrochemical cycles (C1, D1, C2, and D2), as shown in Figure 3 and Figure S5. The evolution of the Fe K-edge in both MnHCF-P and MnHCF-A electrodes is quite reversible. The XANES curves of the charged electrodes (C1 and C2) are shifted toward higher energies (
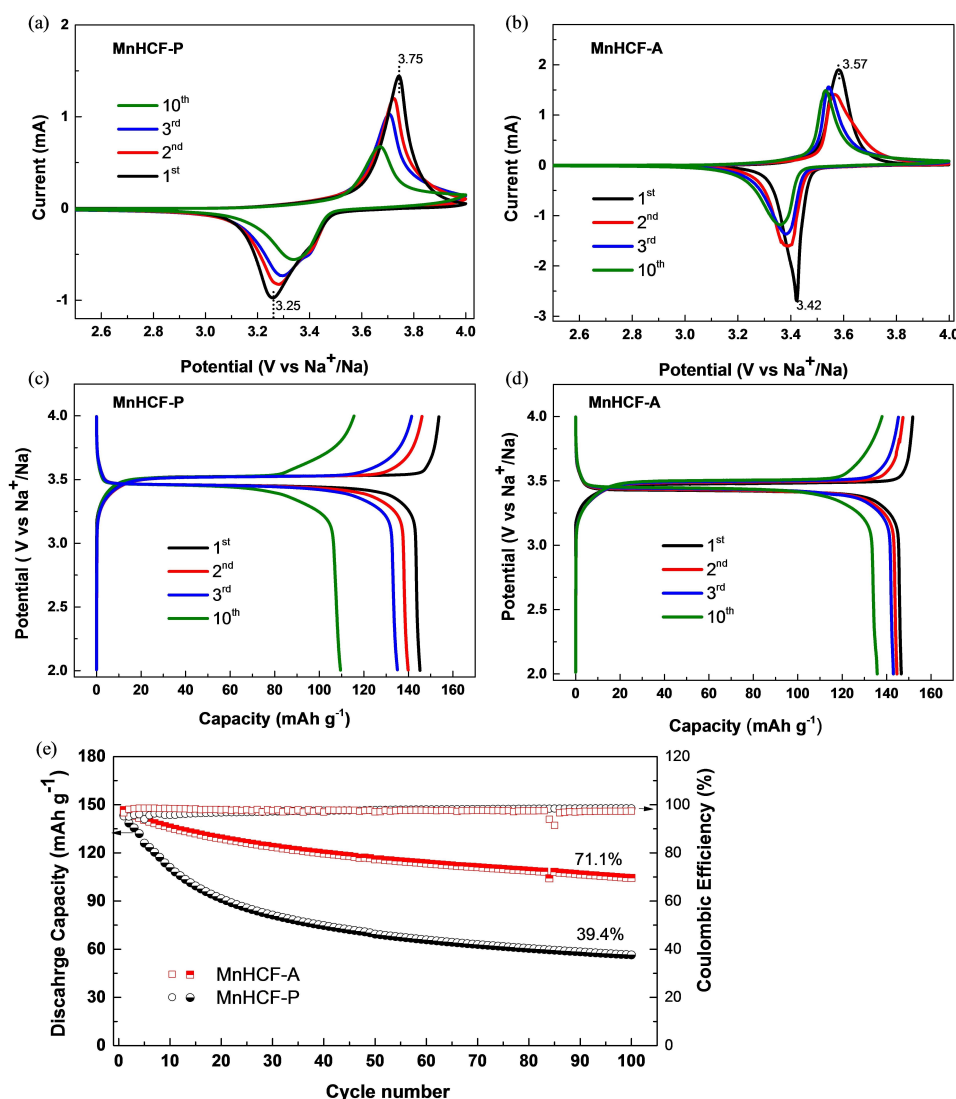
**ChemSusChem**

Research Article
doi.org/10.1002/cssc.202300201

**Chemistry
Europe**

European Chemical
Societies Publishing

**Figure 2.** (a, b) CV curves of MnHCF-P/A electrodes at 0.2 mV s$^{-1}$ during the 1$^{st}$, 2$^{nd}$, 3$^{rd}$ and 10$^{th}$ cycle. (c, d) Galvanostatic charge/discharge curves of MnHCF-P/A at C/5 during the 1$^{st}$, 2$^{nd}$, 3$^{rd}$ and 10$^{th}$ cycle. (e) Discharge capacity and coulombic efficiency upon long-term galvanostatic cycling (100 cycles) of MnHCF-P/A at C/5 rate.

$\approx 1$ eV at the absorption unity in the rising edge), comparing with the discharged states (D1 and D2) and the pristine electrodes. From the FT of the EXAFS spectra at the Fe K-edge for both MnHCF-P and MnHCF-A, an obvious difference is observed between the third peak of the charged and discharged electrodes, which correspond to the 3$^{rd}$ shell, the Mn (Figure S5c, d). Thus, we anticipate relevant difference affecting the Mn XAS spectra. As shown in Figure 3a and b, the edge shift of the Mn K-edge is more significant than that of the Fe K-edge at charged states, which is due to the charge effect combined with the local structural changes (JT-distortion) operating exclusively at the Mn sites. However, a different picture is observed for MnHCF-A, as Figure 3b and Figure S5b report. The Fe K-edge is reversible at the charged states, while the Mn K-edge displays a different shape and energy shift at C1 and C2 states, which can be resulted from different factors, i.e., the oxidation state, the spin state and the ligands impact. The

relative FTs at Mn K-edge show totally different peaks between the charged states and discharged states, which indicates the surrounding environment of Mn sites is different at charged and discharged states. XANES spectra alone cannot be conclusive here; therefore, a more detailed EXAFS analysis was performed to reveal the local structural changes.

The results are detailed in Table S1 and Figures S6 and S7, and the first shell distances of the Mn sites (Mn–N) are compared in Figure 3e for all the electrodes. The Mn environment in the pristine electrode consists of a symmetric MnN$_6$ octahedra, with the Mn–N distance being 2.18 Å and 2.19 Å for MnHCF-P and MnHCF-A, respectively. After the first charge, the four equatorial Mn–N distances contract to 1.95 Å and 1.96 Å for MnHCF-P and MnHCF-A electrodes, respectively, i.e., shrinking by 10.55% and 10.50%, respectively. Meanwhile, the axial Mn–N distances remain roughly constant. However, a more insightful point is the comparison of the Mn–N distance at the
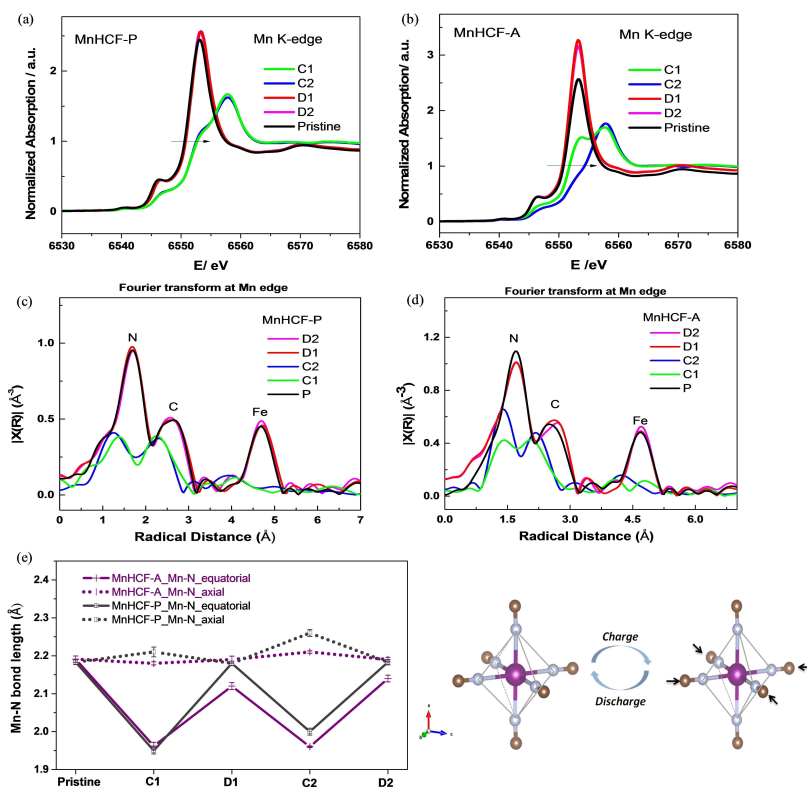
**ChemSusChem**

Research Article
doi.org/10.1002/cssc.202300201

**Chemistry Europe**
European Chemical
Societies Publishing

**Figure 3.** (a, b) Ex-situ XANES spectra of Mn K-edge for MnHCF-P/A samples. (c, d) Corresponding Fourier transforms of $k^2$-weighted EXAFS signals at Mn K-edge. (e) Evolution of Mn first shell: Mn–N distances in both axial and equatorial direction for MnHCF-P/A samples at different charge states.

discharged state. For MnHCF-P electrodes, the $MnN_6$ unit structure recovers quite well to the octahedral symmetry's configuration, with all the Mn–N bond distances sharing the same value in both axial and equatorial directions. On the contrary, the MnHCF-A electrodes experience an irreversible configuration change after the 1st charge and discharge cycle, which is also kept for the 2nd cycle, with the 4 equatorial Mn–N bonds being always shorter than the axial ones. This irreversible change respect, however, enables MnHCF-A electrodes to undergo less local structure variation during the charge and discharge process. In fact, based on the data above, the low-vacancy-content MnHCF-A experiences less effect from the JT-distortion and less structural variations during charge/discharge process.

To obtain more information about the changes of crystal structure in cycled electrodes and to better explain the different electrochemical performance of MnHCF-P and MnHCF-A, ex situ synchrotron XRD patterns of the two materials were collected also after 10 cycles. As observed in Figure 4a and b, a reversible change of XRD patterns between charged (C1, C2, C10) and discharged (D1, D2, D10) electrodes is observed, in both MnHCF-P and MnHCF-A electrodes. After the first charge process, the pristine peaks at 1.20 Å$^{-1}$ and 2.40 Å$^{-1}$ split into two peaks at around 1.20/1.24 Å$^{-1}$ and 2.40/2.49 Å$^{-1}$, respectively. The peaks at around 1.68 Å$^{-1}$ and 1.71 Å$^{-1}$ disappeared and were replaced by a single peak at 1.73 Å$^{-1}$. These changes indicate the potential of a phase change after charge. Based on

reports,[14,27,31,39] the monoclinic MnHCF phase, normally, experiences a phase transformation upon extraction of $Na^+$: from monoclinic to cubic and then tetragonal phase. To get a detailed and quantitative insight into the structural changes of the two materials, Pawley refinement was conducted on all the cycled electrodes.

Due to the similar XRD pattern of the all the discharged electrodes to the pristine one, a Pawley refinement was conducted using the monoclinic ($P21/n$) phase. For all the charged electrodes, the refinement attempt was first carried out by adopting tetragonal ($I-4m2$) phase, a phase mentioned in most articles,[27] and the fitting results are shown in Figure 4d–f, Figure S8 and Table S2. For a pure tetragonal phase, the $a/c$ ratio can be fixed to 0.7071,[31] typically, if effects from JT distortion are excluded. The refinement results in Figure 4e show that both MnHCF-P and MnHCF-A electrodes display a lower value, i.e., $(a/c)_{MnHCF-A} < (a/c)_{MnHCF-P} < 0.7071$, indicating that both MnHCF-P and MnHCF-A electrodes exhibit a distorted tetragonal phase in the charged state, especially the MnHCF-A electrode. The analysis of the $b$ value and volume for both electrodes display a reversible decreasing and increasing values upon charging (de-sodiation) and discharging (sodiation). The volume of the MnHCF-A electrode is slightly less changing than that of the MnHCF-P electrode, decreasing by 6.4%/5.8%/5.3% with respect to 7.6%/7.6%/7.7%, respectively, at each charge states. This provides evidence of a lower volume variation of
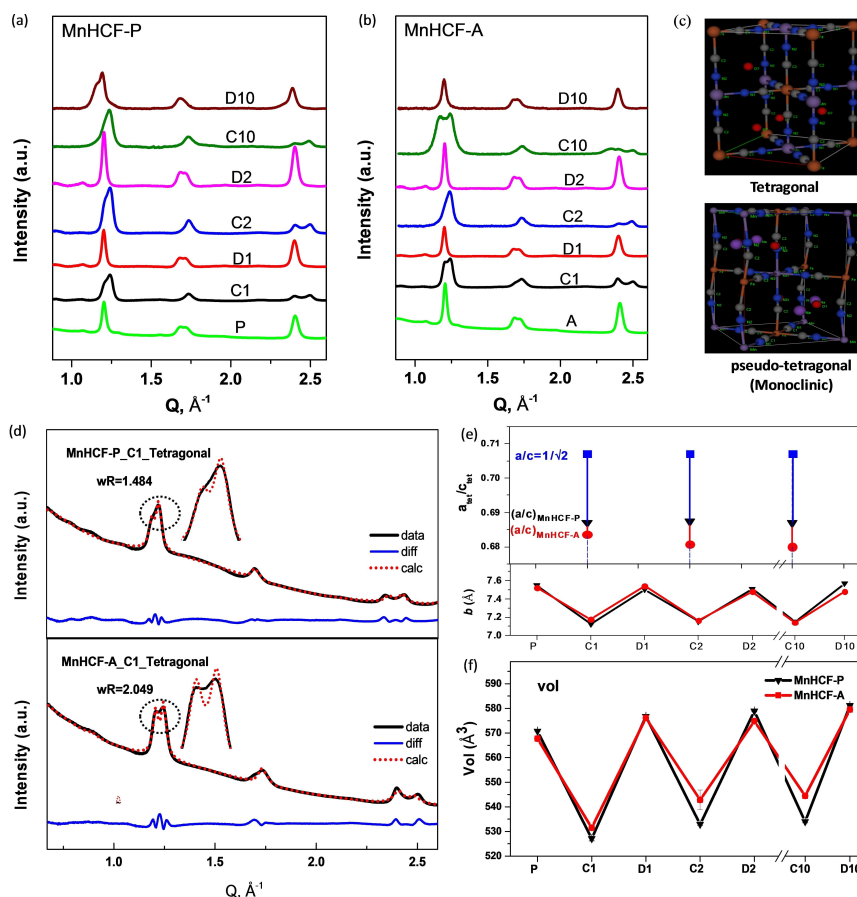
**ChemSusChem**

Research Article
doi.org/10.1002/cssc.202300201

**Chemistry Europe**
European Chemical
Societies Publishing

**Figure 4.** Ex-situ XRD patterns of MnHCF-P (a) and MnHCF-A (b) at different charge-discharge states (C1, D1, C2, D2 and C10, D10). (c) Crystal structure of tetragonal phase and pseudo-tetragonal (monoclinic) phase. (d) Pawley refinement of MnHCF-P and MnHCF-A C1 electrodes based on tetragonal phase. (e) $a_{tet}/c_{tet}$ value of MnHCF-P and MnHCF-A at charge states, as well as the change of $b$ values. (f) Volume change of MnHCF-P and MnHCF-A at different charge and discharge states. Results were refined based on tetragonal phase.

MnHCF-A structure from monoclinic phase to the distorted tetragonal phase, which is required for the charged electrodes.

Being the crystalline phase of all electrodes in the charged state not an ideal tetragonal phase, another refinement was conducted using the pseudo-tetragonal phase, which is a monoclinic phase with a beta ($\beta$) value very close to 90°. The fitting outcomes are shown in Figure 5, Figure S9 and reported in Table S3. As observed, the distorted monoclinic phase exhibits better fitting results than the tetragonal phase. The cell parameters, beta value and volume exhibit the same change trend as the results from the tetragonal phase, decreasing upon charge and increasing during discharge. In particular, the variation of the $\beta$ values (Figure 5d) of the MnHCF-P electrode during charge/discharge process is larger than for the MnHCF-A electrode, indicating that a rather larger structure rearrangement is required by the Na$^+$ extraction/insertion in MnHCF-P samples.

Combing the EXAFS results and XRD results, it is found that the extraction of Na$^+$ from MnHCF-P and MnHCF-A electrodes induces a local contraction of Mn–N equatorial distance. Correspondingly, the cell parameters and volume value exhibit the same decreasing tend, while just MnHCF-A has relatively smaller changes. This contraction is due to the local strain caused by the oxidation of Mn$^{2+}$ (0.83 Å) to Mn$^{3+}$ (0.65 Å), as well as the JT-distortion of Mn$^{3+}$.[24,40] Thus, a cooperative JT distortion, which was proposed by Goodenough and co-workers[14] and Jiang and coworkers[27] during the phase evolution of MnHCF, is confirmed to occur in both MnHCF-P/A. However, differently from MnHCF-P sample, the extraction of Na$^+$ from MnHCF-A induces a weaker distortion at the Mn sites, as well as a relatively smaller crystal modification during the charge/discharge process, which could be the reasons for the better electrochemical performance of MnHCF-A electrodes. From the vacancy content perspective, the structure of MnHCF-A, which displays a minor content of vacancy, is also structurally more "rigid" favoring a mitigation of the JT effect. On the contrary, the structure with a higher vacancy content, as for MnHCF-P, even though potentially more flexible for the presence of more space inside the polymeric –Mn–N–C–Fe– structural framework, is not effective in the mitigation of JT effect. Indeed, this "more space" is used not only to accommodate the JT structural deformation, but also as an alternative intercalation site for Na$^+$ ions. This competition, in turn, is not favoring the electrochemical performance.
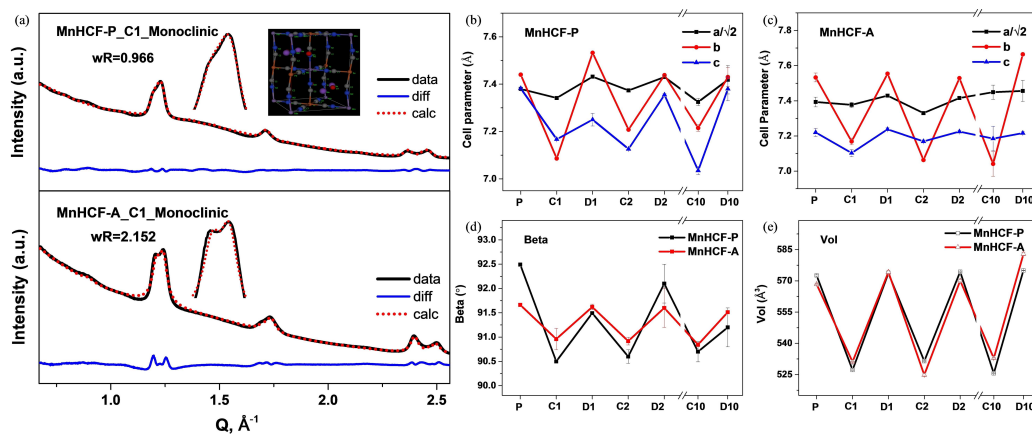
**ChemSusChem**

Research Article
doi.org/10.1002/cssc.202300201

**Chemistry**
**Europe**
European Chemical
Societies Publishing

**Figure 5.** (a) Pawley refinement of MnHCF-P and MnHCF-A C1 electrodes based on monoclinic phase. (b, c) Cell parameters (*a, b, c*) of MnHCF-P and MnHCF-A electrodes, as well as the comparison of (d) beta (*β*) value and (e) volume of MnHCF-P and MnHCF-A at different charge and discharge states. Results were refined based on monoclinic phase.

## Conclusion

Two manganese hexacyanoferrates (MnHCF) materials with relatively higher and lower vacancy content, denoted as MnHCF-P and MnHCF-A, respectively, were synthesized and their Na-ion storage performance was characterized extensively. The electrochemical results indicate that the sample with the lowest vacancy content (4%) exhibits the best cycling stability with 71.1% capacity retention after 100 cycles at C/5 rate. The ex situ X-ray absorption spectroscopy (XAS) data show that the MnHCF-A electrode experiences an irreversible local configuration change at Mn sites during the charge/discharge process, which in turn involves less local structure variation during the charge and discharge process compared to MnHCF-P. As a result, the MnHCF-A electrode show a weaker Jahn-Teller (JT) distortion effect. Additionally, reversible ex situ X-ray diffraction (XRD) patterns between the charge and discharge state for both MnHCF-P and MnHCF-A electrodes were observed. The refinements of all charged electrodes were conducted with two phases: tetragonal and pseudo-tetragonal (monoclinic) phase. The fitting results display that a cooperative JT-distortion effect occur in both MnHCF-P and MnHCF-A electrodes. Another piece of evidence suggested that the MnHCF-P electrode experienced more configuration rearrangement (volume or *β* value) in charged and discharged state electrodes. Overall, the better electrochemical performance of MnHCF-A electrode is explained by the weak JT-distortion effect resulting in a stable crystal structure during Na$^+$ release and insertion.

## Conflict of Interest

The authors declare no conflict of interest.

## Data Availability Statement

The data that support the findings of this study are available on request from the corresponding author. The data are not publicly available due to privacy or ethical restrictions.

**Keywords:** manganese hexacyanoferrate · organic Na-ion battery · vacancy content · cycling stability · Jahn-Teller distortion

[1] T. Matsuda, Y. Moritomo, *Appl. Phys. Express* **2011**, *4*, 4–7.
[2] C. D. Wessells, S. V. Peddada, R. A. Huggins, Y. Cui, *Nano Lett.* **2011**, *11*, 5421–5425.
[3] M. Pasta, C. D. Wessells, R. A. Huggins, Y. Cui, *Nat. Commun.* **2012**, *3*, 1149.
[4] L. Wang, Y. Lu, J. Liu, M. Xu, J. Cheng, D. Zhang, J. B. Goodenough, *Angew. Chem. Int. Ed.* **2013**, *52*, 1964–1967; *Angew. Chem.* **2013**, *125*, 2018–2021.
[5] A. Eftekhari, *J. Power Sources* **2004**, *126*, 221–228.
[6] Y. Kurihara, T. Matsuda, Y. Moritomo, *Jpn. J. Appl. Phys.* **2013**, *52*, 017301.
[7] T. Matsuda, M. Takachi, Y. Moritomo, *Chem. Commun.* **2013**, *49*, 2750–2752.
[8] L. Xue, Y. Li, H. Gao, W. Zhou, X. Lü, W. Kaveevivitchai, A. Manthiram, J. B. Goodenough, *J. Am. Chem. Soc.* **2017**, *139*, 2164–2167.
[9] Y. Sun, C. Liu, J. Xie, D. Zhuang, W. Zheng, X. Zhao, *New J. Chem.* **2019**, *43*, 11618–11625.
[10] Y. Mizuno, M. Okubo, E. Hosono, T. Kudo, K. Oh-Ishi, A. Okazawa, N. Kojima, R. Kurono, S. I. Nishimura, A. Yamada, *J. Mater. Chem. A* **2013**, *1*, 13055–13059.
[11] S. Yagi, M. Fukuda, T. Ichitsubo, K. Nitta, M. Mizumaki, E. Matsubara, *J. Electrochem. Soc.* **2015**, *162*, A2356–A2361.

**ChemSusChem**

Research Article
doi.org/10.1002/cssc.202300201

**Chemistry Europe**
European Chemical
Societies Publishing

[12] W. Li, C. Xu, X. Zhang, M. Xia, Z. Yang, H. Yan, H. Yu, L. Zhang, W. Shu, J. Shu, *J. Electroanal. Chem.* **2021**, *881*, 114968.

[13] D. Wang, H. Lv, T. Hussain, Q. Yang, G. Liang, Y. Zhao, L. Ma, Q. Li, H. Li, B. Dong, T. Kaewmaraya, C. Zhi, *Nano Energy* **2021**, *84*, 105945.

[14] J. Song, L. Wang, Y. Lu, J. Liu, B. Guo, P. Xiao, J. J. Lee, X. Q. Yang, G. Henkelman, J. B. Goodenough, *J. Am. Chem. Soc.* **2015**, *137*, 2658–2664.

[15] A. Mullaliu, J. Asenbauer, G. Aquilanti, S. Passerini, M. Giorgetti, *Small Methods* **2020**, *4*, 1900529.

[16] A. Zhou, Z. Xu, H. Gao, L. Xue, J. Li, J. B. Goodenough, *Small* **2019**, *15*, 1–6.

[17] M. H. Alfaruqi, V. Mathew, J. Gim, S. Kim, J. Song, J. P. Baboo, S. H. Choi, J. Kim, *Chem. Mater.* **2015**, *27*, 3609–3620.

[18] S. Islam, M. H. Alfaruqi, V. Mathew, J. Song, S. Kim, S. Kim, J. Jo, J. P. Baboo, D. T. Pham, D. Y. Putro, Y. K. Sun, J. Kim, *J. Mater. Chem. A* **2017**, *5*, 23299–23309.

[19] M. D. Radin, A. Van Der Ven, *Chem. Mater.* **2018**, *30*, 607–618.

[20] X. Li, Y. Xu, C. Wang, *J. Alloys Compd.* **2009**, *479*, 310–313.

[21] C. Zuo, Z. Hu, R. Qi, J. Liu, Z. Li, J. Lu, C. Dong, K. Yang, W. Huang, C. Chen, Z. Song, S. Song, Y. Yu, J. Zheng, F. Pan, *Adv. Energy Mater.* **2020**, *10*, 1–10.

[22] H. Kim, G. Yoon, I. Park, K. Y. Park, B. Lee, J. Kim, Y. U. Park, S. K. Jung, H. D. Lim, D. Ahn, S. Lee, K. Kang, *Energy Environ. Sci.* **2015**, *8*, 3325–3335.

[23] Y. Moritomo, S. Urase, T. Shibata, *Electrochim. Acta* **2016**, *210*, 963–969.

[24] M. Oliver-Tolentino, M. González, H. Osiry, G. Ramos-Sánchez, I. González, *Dalton Trans.* **2018**, *47*, 16492–16501.

[25] W. Li, C. Han, W. Wang, Q. Xia, S. Chou, Q. Gu, B. Johannessen, H. K. Liu, S. Dou, *Adv. Energy Mater.* **2020**, *10*, 1–11.

[26] S. S. Chou, F. Gebert, D. L. Cortie, J. C. Bouwer, W. Wang, Z. Yan, S.-X. S. S.-X. Dou, S. S. Chou, *Angew. Chem. Int. Ed.* **2021**, *60*, 18519–18526; *Angew. Chem.* **2021**, *133*, 18667–18674.

[27] Y. Tang, W. Li, P. Feng, M. Zhou, K. Wang, Y. Wang, K. Zaghib, K. Jiang, *Adv. Funct. Mater.* **2020**, *30*, 1–9.

[28] A. Mullaliu, M. Gaboardi, J. R. Plaisier, S. Passerini, M. Giorgetti, *ACS Appl. Energ. Mater.* **2020**, *3*, 5728–5733.

[29] S. Kjeldgaard, M. Wagemaker, B. B. Iversen, A. Bentien, *Mater Adv* **2021**, *2*, 2036–2044.

[30] T. Hosaka, T. Fukabori, H. Kojima, K. Kubota, S. Komaba, *ChemSusChem* **2021**, *14*, 1166–1175.

[31] Y. Shang, X. Li, J. Song, S. Huang, Z. Yang, Z. J. Xu, H. Y. Yang, *Chem* **2020**, *6*, 1804–1818.

[32] B. H. Toby, R. B. Von Dreele, *J. Appl. Crystallogr.* **2013**, *46*, 544–549.

[33] G. Aquilanti, M. Giorgetti, R. Dominko, L. Stievano, I. Arčon, N. Novello, L. Olivi, I. Ar, N. Novello, L. Olivi, I. Arčon, N. Novello, L. Olivi, *J. Phys. D* **2017**, *50*, 074001.

[34] B. Ravel, M. Newville, *J. Synchrotron Radiat.* **2005**, *12*, 537–541.

[35] Y. You, X. Yu, Y. Yin, K. W. Nam, Y. G. Guo, *Nano Res.* **2015**, *8*, 117–128.

[36] H. A. Tajmir-Riahi, *J. Inorg. Biochem.* **1991**, *42*, 47–55.

[37] G. Ni, Z. Hao, G. Zou, X. Xu, B. Hu, F. Cao, C. Zhou, *Sustain. Energy Fuels* **2022**, *6*, 1353–1361.

[38] M. Li, R. Sciacca, M. Maisuradze, G. Aquilanti, J. Plaisier, M. Berrettoni, M. Giorgetti, *Electrochim. Acta* **2021**, *400*, 139414.

[39] H. Wang, E. Xu, S. Yu, D. Li, J. Quan, L. Xu, L. Wang, Y. Jiang, *ACS Appl. Mater. Interfaces* **2018**, *10*, 34222–34229.

[40] M. Pasta, R. Y. Wang, R. Ruffo, R. Qiao, H. W. Lee, B. Shyam, M. Guo, Y. Wang, L. A. Wray, W. Yang, M. F. Toney, Y. Cui, *J. Mater. Chem. A* **2016**, *4*, 4211–4223.